Simulation and Modeling of Hypersonic Turbulent Boundary Layers Subject to Adverse Pressure Gradients due to Concave Streamline Curvature

Gary L. Nicholson*, Junji Huang† and Lian Duan‡
The Ohio State University, Columbus, OH 43210

Meelan M. Choudhari§
NASA Langley Research Center, Hampton, VA 23681

Direct numerical simulations (DNS) of adverse-pressure-gradient turbulent boundary layers over a planar concave wall are presented for a nominal freestream Mach number of 5, with the objective of assessing the limitations of the currently available Reynolds-averaged Navier-Stokes (RANS) models. The wall geometry and flow conditions of the DNS are representative of the experimental data for a Mach 4.9 turbulent boundary layer that was tested on a two-dimensional planar concave wall model in the high-speed blow-down wind tunnel located at the National Aerothermochemistry Laboratory at Texas A&M University (TAMU). The DNS was validated against the experimental results of TAMU for the same flow conditions and wall geometry. An analysis of the DNS datasets was also conducted to provide an assessment of the validity of Morkovin's hypothesis and the strong Reynolds analog for turbulence subject to mechanical nonequilibrium. In addition to the DNS results, RANS predictions are obtained by using the Baldwin-Lomax (BL), Spalart-Allmaras (SA), and the $k-\omega$ SST turbulence models. The comparisons between RANS and DNS showed little impact of an adverse pressure gradient on the accuracy of these models, at least up to an incompressible Clauser pressure gradient parameter of $\beta_{inc} = 1.22$ While the Boussinesq assumption provided reasonable predictions for the Reynolds shear stress, it failed to adequately predict the normal components of the Reynolds stress.

Nomenclature

B_q = wall heat transfer rate, $B_q = q_w/(\rho_w C_p u_\tau T_w)$, dimensionless
C_f = wall skin friction coefficient, $C_f = \tau_w/(\frac{1}{2}\rho_\infty U_\infty^2)$, dimensionless
C_h = wall heat flux coefficient, $C_h = q_w/\left(\rho_\infty C_p U_\infty (T_r - T_w)\right)$, dimensionless
C_p = heat capacity at constant pressure, J/(K·kg)
C_v = heat capacity at constant volume, J/(K·kg)
E = total energy per unit mass, $E \equiv e + \frac{1}{2}u_i u_i$, J/kg
H = shape factor, $H \equiv \delta^*/\theta$, dimensionless
M = Mach number, $M \equiv u/a$, dimensionless
M_τ = friction Mach number, $M_\tau = u_\tau/(\gamma R T_w)^{1/2}$, dimensionless
N_f = number of fields used to accumulate statistics, dimensionless
Pr = molecular Prandtl number, $Pr = 0.71$, dimensionless
Pr_t = turbulent Prandtl number, $Pr_t \equiv \left(\overline{\rho u'' w''}(\partial\tilde{T}/\partial z)\right)/\left(\overline{\rho w'' T''}(\partial\tilde{u}/\partial z)\right)$, dimensionless
R = ideal gas constant, $R = 287$, J/(K·kg)
Re_θ = Reynolds number based on momentum thickness and freestream viscosity, $Re_\theta \equiv \rho_\infty u_\infty \theta/\mu_\infty$, dimensionless
$Re_{\delta 2}$ = Reynolds number based on momentum thickness and wall viscosity, $Re_{\delta_2} \equiv \rho_\infty u_\infty \theta/\mu_w$, dimensionless
Re_τ = Reynolds number based on shear velocity and wall viscosity, $Re_\tau \equiv \rho_w u_\tau \delta/\mu_w$, dimensionless

*Graduate Student, Department of Mechanical and Aerospace Engineering, Student Member, AIAA
†Graduate Student, Department of Mechanical and Aerospace Engineering, Student Member, AIAA
‡Associate Professor, Department of Mechanical and Aerospace Engineering, Senior Member, AIAA
§Aerospace Technologist, Computational AeroSciences Branch, M.S. 128. Fellow, AIAA

Re^*_τ = semilocal Reynolds number, $Re^*_\tau \equiv \sqrt{\tau_w/\rho_\infty}\delta/\nu_\infty$, dimensionless
S_{ij} = rate-of-strain tensor, $S_{ij} = \frac{1}{2}\left(\frac{\partial u_i}{\partial x_j} + \frac{\partial u_j}{\partial x_i}\right)$, Hz
T = temperature, K
T_r = recovery temperature, $T_r = T_\infty(1 + 0.89\frac{\gamma-1}{2}M^2_\infty)$, K
t_f = time spanned to accumulate statistics, s
U_∞ = freestream velocity, m/s
a = speed of sound, m/s
e = internal energy per unit mass, $e \equiv C_v T$, J/kg
h = enthalpy per unit mass, $h \equiv C_p T$, J/kg
$\widetilde{k}$ = turbulent kinetic energy, $\widetilde{k} \equiv \widetilde{u''_i u''_i}/2$, J/kg
p = pressure, Pa
q = conductive heat flux, W/m^2
q^T_i = turbulent heat flux term, $q^T_i = \overline{\rho h'' u''_i}$, W/m^2
q_w = wall heat flux, W/m^2
s = entropy, J/(kg·K)
u = streamwise velocity, m/s
u_τ = friction velocity, $u_\tau \equiv \sqrt{\tau_w/\overline{\rho}_w}$, m/s
u^*_τ = density weighted velocity scale, $u^*_\tau \equiv \sqrt{\tau_w/\overline{\rho}} = u_\tau\sqrt{\overline{\rho}_w/\overline{\rho}}$, m/s
v = spanwise velocity, m/s
w = wall-normal velocity, m/s
x = streamwise direction of the local body intrinsic coordinate system, m
x_g = streamwise direction of the right-handed Cartesian coordinate system, m
y = spanwise direction of the local body intrinsic coordinate system, m
y_g = spanwise direction of the right-handed Cartesian coordinate system, m
z = wall-normal direction of the local body intrinsic coordinate system, m
z_g = vertical coordinate that is perpendicular to the plane determined by the x_g- and y_g-coordinates, m
z_τ = viscous length, $z_\tau = \nu_w/u_\tau$, m
z^*_τ = semilocal length scale, $z^*_\tau \equiv \bar{\mu}/(\bar{\rho}u^*_\tau)$, m
β = Clauser pressure gradient parameter, $\beta = (dp/dx)(\delta^*/\tau_w)$, dimensionless
β_{inc} = incompressible Clauser pressure gradient parameter, $\beta_{inc} = (dp/dx)(\delta^*_{inc}/\tau_w)$, dimensionless
I_p = Impulse parameter for bulk dilation, $I_p = \gamma^{-1}\ln(p_2/p_1)$
I_ϕ = Impulse parameter for streamline curvature, $I_\phi = \Delta\phi$
γ = specific heat ratio, $\gamma = C_p/C_v$, dimensionless
δ = boundary-layer thickness (based on 99.5% of the freestream total enthalpy), m
δ^* = displacement thickness, m
κ = von Kármán constant $\kappa = 0.41$, dimensionless
θ = momentum thickness, m
ϑ^T_i = turbulent heat flux term, $\vartheta^T_i = \overline{\rho e'' u''_i}$, W/m^2
μ = dynamic viscosity, $\mu = 1.458\times10^{-6}T^{3/2}/(T + 110.4)$, kg/(m·s)
ν = kinematic viscosity, $\nu = \mu/\rho$, m^2/s
ρ = density, kg/m^3
σ = viscous stress tensor, Pa
τ = shear stress, Pa

Subscripts

i = inflow station for the domain of direct numerical simulations
inc = incompressible variables
rms = root mean square
w = wall variables
∞ = freestream variables

Superscripts

T = turbulent quantities in RANS equations
$+$ = variable in inner wall units, $(\cdot)^+ \equiv (\cdot)/z_\tau$
$\overline{(\cdot)}$ = standard (Reynolds) averaged variable
$\widetilde{(\cdot)}$ = density-weighted (Favre) averaged variable, $\widetilde{(\cdot)} \equiv \overline{\rho(\cdot)}/\overline{\rho}$
$(\cdot)'$ = fluctuations around standard averages
$(\cdot)''$ = fluctuations around Favre averages

I. Introduction

All realistic hypersonic vehicles exhibit some degree of streamline curvature that induces favorable and/or adverse pressure gradients. As such, there is a need to understand how pressure gradients drive the transport of boundary-layer turbulence in the hypersonic regime, so that the underlying physical processes can be accurately modelled and, hence, also utilized to the advantage of vehicle designs.

The existing literature on the effect of streamline curvature on hypersonic boundary-layer turbulence is rather limited, whether in regard to measurements, modeling, or numerical simulations. Most previous studies of fully turbulent boundary layers (TBLs) that included pressure gradients focused on low-speed boundary layers (see, for example, Refs. [1–7]), with considerably fewer studies involving supersonic boundary layers, and even less targeting the hypersonic regime. The existing experiments were largely limited to either single-point measurements of the velocity fluctuations based on hot-wire anemometry and/or laser Doppler velocimetry [8–14] or global measurements of the velocity field by the particle image velocimetry (PIV) [15–24]. While the available measurements have yielded valuable insights into the effect of pressure gradients on the behavior, distribution, and scaling of the mean velocity and the Reynolds-stresses associated with the turbulence field, none of the existing experiments have been able to provide sufficiently well resolved, global measurements of both velocity and thermodynamic fields (including in the immediate vicinity of the wall), so as to facilitate a systematic investigation of the turbulence scaling laws and to enable a detailed evaluation of the underlying modeling assumptions for RANS turbulence models. As far as the high-fidelity simulations such as DNS are concerned, nearly all of the existing DNS have been conducted at freestream Mach numbers of less than 3 [25–30], where the compressibility effects are expected to be too weak to cause any significant deviation of the turbulence statistics from its incompressible behavior.

Recently, Nicholson et al. [31] presented the results of a new, in-depth DNS dataset of nominally Mach 5 TBLs subject to favorable pressure gradients (FPG) due to streamline curvature. The DNS simulation simulated the flow configuration from the experiments performed in the National Aerothermochemistry Laboratory (NAL) at the Texas A&M University, which included zero, weak, and strong favorable pressure gradients induced via appropriately designed surface curvature [18]. The DNS has been validated against the experimental results of Tichenor et al. [18] for both zero and nonzero pressure gradients, as well as through selective comparisons with several other DNS datasets for a ZPG boundary-layer [32–34]. In general, the DNS results agree well with the velocity profiles measured in the experiment. For the ZPG case, the Van Driest II transformed velocities from the DNS show good collapse with other DNS results for a variety of Mach numbers. Consistent with the experiment of Tichenor et al. [18], the DNS predicted a substantial reduction of Reynolds stresses and turbulent heat flux with increasing pressure gradient; and for strong pressure gradient, the shear stress and wall-normal heat flux became nearly zero or even slightly negative in the outer region of the boundary layer, highlighting a decay in the turbulent motion. Both the assumption of a constant Prandtl number and Huang's version of strong Reynolds analogy were found to be adequate for zero and weak FPGs, but failed under the effects of the strong FPG. In addition to characterizing the physics of high-speed turbulence subject to streamline-curvature-driven FPG, the DNS datasets of Nicholson et al. [31] were used to assess the potential limitations in the modeling assumptions of several currently available turbulence models. Specifically, the predictions of the Baldwin-Lomax, Spalart-Allmaras, Wilcox k-ω, and the k-ω SST turbulence models were evaluated against the DNS data set. The comparisons showed that each model performed quite well under weak pressure gradients. However, a strong FPG led to a significant variance among the predictions of those models. Overall, the k-ω SST model performed the best, yielding DNS-like predictions for the skin friction until the flow shifted from a favorable to an adverse pressure gradient. Nicholson et al. [31] found that the Boussinesq assumption provided reasonable predictions of the Reynolds shear stress, but could not adequately predict the streamwise and wall-normal Reynolds Stresses. While the constant turbulent Prandtl number assumption yielded good predictions of the turbulent heat flux in the wall-normal direction, it was not able to capture the turbulent heat transfer in the streamwise direction. These previous results highlight the need for higher-fidelity models that can successfully capture the transport of Reynolds stresses and all components of the

turbulent heat flux. One such model is the algebraic energy flux, AEF, model by Bowersox [35], which has recently shown promising results. The studies of hypersonic TBLs subject to streamline-curvature-driven pressure gradients and the assessments of turbulence models for such flows have been limited to those with FPG. A similar study for hypersonic TBLs with adverse pressure gradients is lacking. This important technical gap is targeted in the current paper.

The primary objective of this paper is to extend the DNS database of Nicholson et al. [31] to hypersonic TBLs subjected to APG. Specifically, we will present the results of a new DNS of a nominally Mach 5 APG TBL that simulates the experimental flow configuration from Neel et al. [36]. In particular, the current study will extend the assessment of the assumptions underlying the AEF model of Boxersox for high-speed TBLs subject to streamline-curvature-driven APG.

The paper is structured as follows. The flow conditions and numerical methodology are outlined in Section II and III, respectively. While section IV presents a comparison of the DNS results against the experiments of TAMU of streamline curvature-driven APG TBLs at Mach 4.9; and section V provides an assessment of several Reynolds stress and turbulent heat flux formulations for the RANS of hypersonic TBLs against the DNS results. A summary of the paper is given in Section VI.

II. Flow Conditions

The present work targets both DNS and RANS computations of streamline-curvature-driven APG TBLs with an incoming Mach number of 4.9. The flow conditions are selected to match the experiments by Tichenor et al. [18], while the wall geometry has been selected to match those from the experiment by Tichenor et al. [20] in the National Aerothermochemistry Laboratory (NAL) at the Texas A&M University. This results in a small difference of the freestream conditions used with respect to those from Tichenor et al. [20]. However, this choice was made so that the results from this study can be readily compared with those of an ongoing DNS study[31] that models the FPG experiments of Tichenor et al. [18]. The wall geometry in the experiment by Tichenor et al. [20] consisted of a tunnel wall with a changeable floor insert that could be varied from a flat wall with zero pressure gradient to a curved surface inducing an adverse pressure gradient. Table 1 outlines the freestream and wall-temperature conditions for the cases of interest during the present work. The DNS simulates a baseline ZPG TBL region over a flat plate followed by an APG TBL developing spatially over a concave wall geometry that is defined by an 8-degree arc of a circle with a 50.8 cm radius, followed by an inverted arc that is used to return the tunnel wall to a horizontal contour. This wall geometry is the same as that of the APG model investigated during the TAMU experiment and is shown in Figure 1. The experiments had three sample locations labeled as U, D1, and D2, which are located at an x_g of 0.154 m, 0.292 m, and 0.308 m, respectively. These locations correspond to a location upstream (U) of the curved wall that corresponds to a ZPG TBL, and two locations (D1 and D2) downstream of the starting point of the curved wall. The locations D1 and D2 correspond to APG TBLs.

Table 1 Freestream and wall-temperature conditions for Mach 4.9 DNS cases in comparison with the experiment of Tichenor et al. [20]. δ_i is the boundary-layer thickness at the inflow of Box 1 DNS ($x_g = -0.35$ m) as shown in Figure 2.

Case	M_∞	U_∞, m/s	ρ_∞, kg/m^3	T_∞, K	T_w, K	T_w/T_r	T_r	δ_i, mm
DNS	4.9	794.0	0.272	66.2	317.0	0.91	348	4.0
Exp	4.9	794.9	0.265	65.5	$\approx$ 321.0	1.01	317	-

III. DNS of Hypersonic Turbulent Boundary Layers

To perform the DNS of turbulent boundary layers, the compressible Navier-Stokes equations in conservation form are solved numerically. The inviscid fluxes of the governing equations in curvilinear coordinates are computed by using a seventh-order weighted essentially nonoscillatory (WENO) scheme. The viscous fluxes are discretized with a fourth-order central difference scheme and the time integration is performed by using a third-order, low-storage, Runge-Kutta scheme [37].

Figure 2 shows the computational domain for the DNS. The computations are carried out in three overlapping streamwise domains. Boxes 1 and 2 simulate the ZPG TBL over a flat plate, while box 3 simulates the TBL over a curved

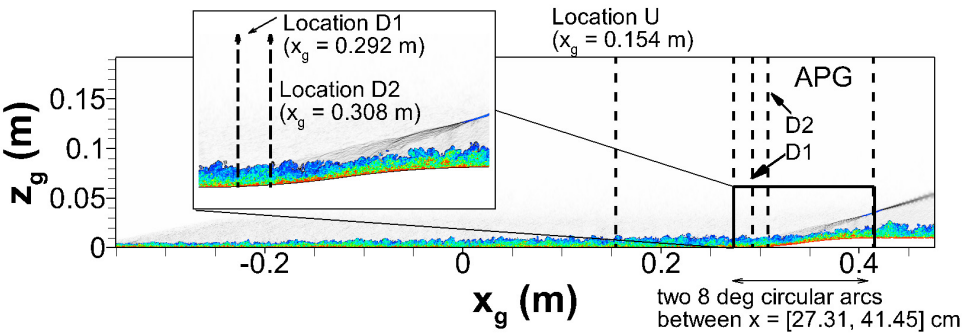

Fig. 1 Schematic of the DNS case M5APG. The grey contours correspond to numerical schlieren, whereas the color contours represent the vorticity magnitude and are intended to highlight the large-scale motions within the boundary layer. Locations U, D1, and D2 denote the measurement locations corresponding to x_g = 0.154 m, 0.292 m, and 0.308 m respectively. The curved wall is defined by two 8-degree arcs that begin and end at 0.2731 m and 0.4145 m, respectively.

wall geometry that produces an adverse pressure gradient. The three boxes have a combined extent of $L_x = 206.5\delta_i$, $L_y = 7\delta_i$, $L_z = 50\delta_i$ in the streamwise(x_g), spanwise(y_g) and wall normal(z_g) directions, respectively, where δ_i is the boundary layer thickness at the inflow of the Box 1 DNS. The grids in the wall normal direction are clustered near the wall, with $z^+_{min} \lesssim 0.6$ at the first grid point away from the wall and the grid spacing near the boundary layer edge is kept uniform with $z^+_{max} \lesssim 9.3$. Details of the grid dimensions, domain size and resolutions are listed in Table 2.

In Box 1, i.e., the ZPG region, a modified rescaling/recycling method [38] is used to generate inflow turbulence, with the recycling station set at $69.3\delta_i$ downstream of the inlet. The selected recycling length falls within the range required to accommodate the eddy decorrelation length and to minimize the effect of inlet transients associated with the recycling process. According to Simens et al. [39], this range corresponds to approximately $30\delta_i$ to $99\delta_i$. The inflow location of the Box 1 DNS is more than $125\delta_i$ upstream of the first sampling location at $x_g = 0.154$ m (labeled as Location U in the experiment [19]) so that the DNS can achieve a fully developed equilibrium state of a ZPG TBL at the sampling location. The computational setup for Box 1 DNS and, also, for the downstream simulations is sketched in Figure 2.

For both the ZPG and APG boxes, no-slip conditions are applied for the three velocity components at the wall and isothermal wall conditions are used for the temperature, with $T_w = 317K$. At the top and the outflow boundaries, unsteady nonreflecting boundary conditions based on Thompson [40] are imposed, and periodic boundary conditions are used in the spanwise direction. The DNS methodology has been extensively validated in previous work for spatially developing supersonic/hypersonic turbulent boundary layers [32, 38, 41–43].

For the current spatial simulations, the boundary-layer grows slowly in the streamwise direction, the boundary-layer thickness δ increases by a factor of approximately three prior to the APG region (Figure 3). As part of this evolution, the friction Reynolds number Re_τ increases from approximately 500 at the inlet $x_g = -0.35$ m to approximately 1150 at the location where the curvature begins. The streamwise computational domain is large enough to allow the memory of the inflow generation to fade out, so that the DNS predicted boundary-layer thickness δ and Clauser equilibrium pressure

Table 2 Summary of parameters for DNS database. $L_\alpha, \alpha = x, y, z$ are the domain sizes in streamwise, spanwise, and wall-normal directions, respectively. N_x, N_y, and N_z are the grid dimensions. Δx^+ and Δy^+ are the uniform grid spacings in the streamwise and spanwise directions. Δz^+ denotes the wall-normal spacing at the first grid point away from the wall and that near the boundary-layer edge. The superscript "+" denotes normalization by the viscous length z_τ at $x_g = 0.0$ m for Boxes 1 and 2 and at Location D1 ($x_g = 0.292$ m) for Box 3, as in Table 3.

Dataset	x_{beg}-x_{end}, m	Δx^+	Δy^+	Δz^+	L_x/δ_i	L_y/δ_i	L_z/δ_i	$N_x \times N_y \times N_z$	$T_f u_\tau/\delta$
Box1,ZPG	-0. 350-0. 073	6.9	5.2	0. 56-8. 8	69.3	7.0	50.0	$4500 \times 600 \times 550$	10.9
Box2,ZPG	-0. 085-0. 191	6.9	5.2	0. 56-8. 8	69.3	7.0	50.0	$4500 \times 600 \times 550$	6.1
Box3,APG	0. 077-0. 476	7.3	5.5	0. 59-9. 3	99.7	7.0	50.0	$6500 \times 600 \times 550$	2.5

gradient parameter β show good comparison with the experimentally measured values upstream of the curvature at all 3 locations

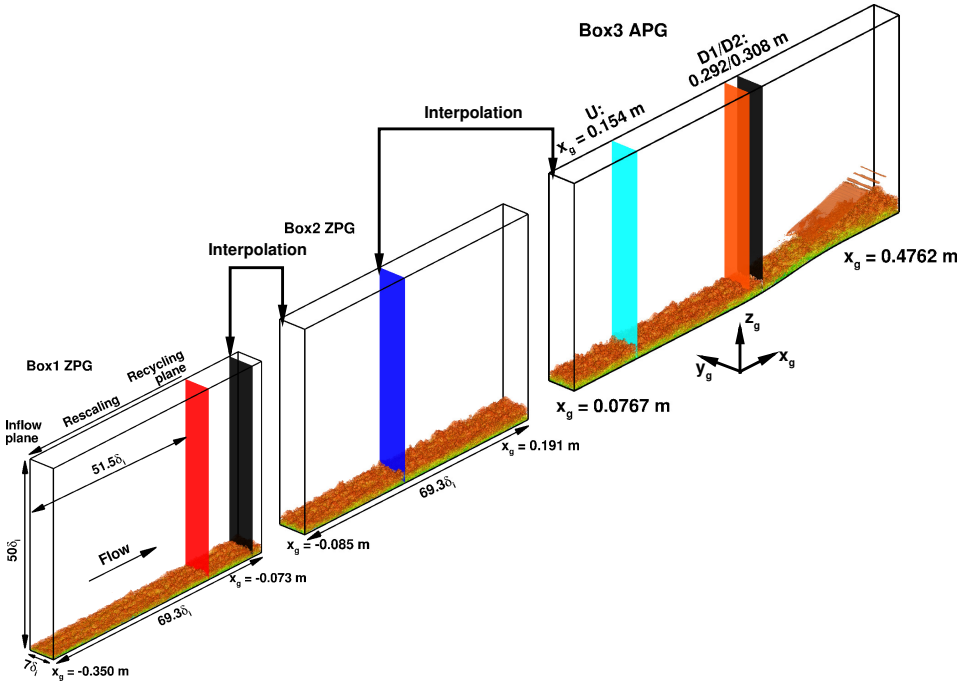

Fig. 2 Computational domain and simulation setup for Mach 5 DNS over wall models of APG case. The instantaneous flow is shown by the isosurface of the magnitude of the density gradient, $|\nabla\rho|\delta_i/\rho_\infty \approx 0.98$ and colored by the streamwise velocity component (with levels from 0 to U_∞, blue to red).

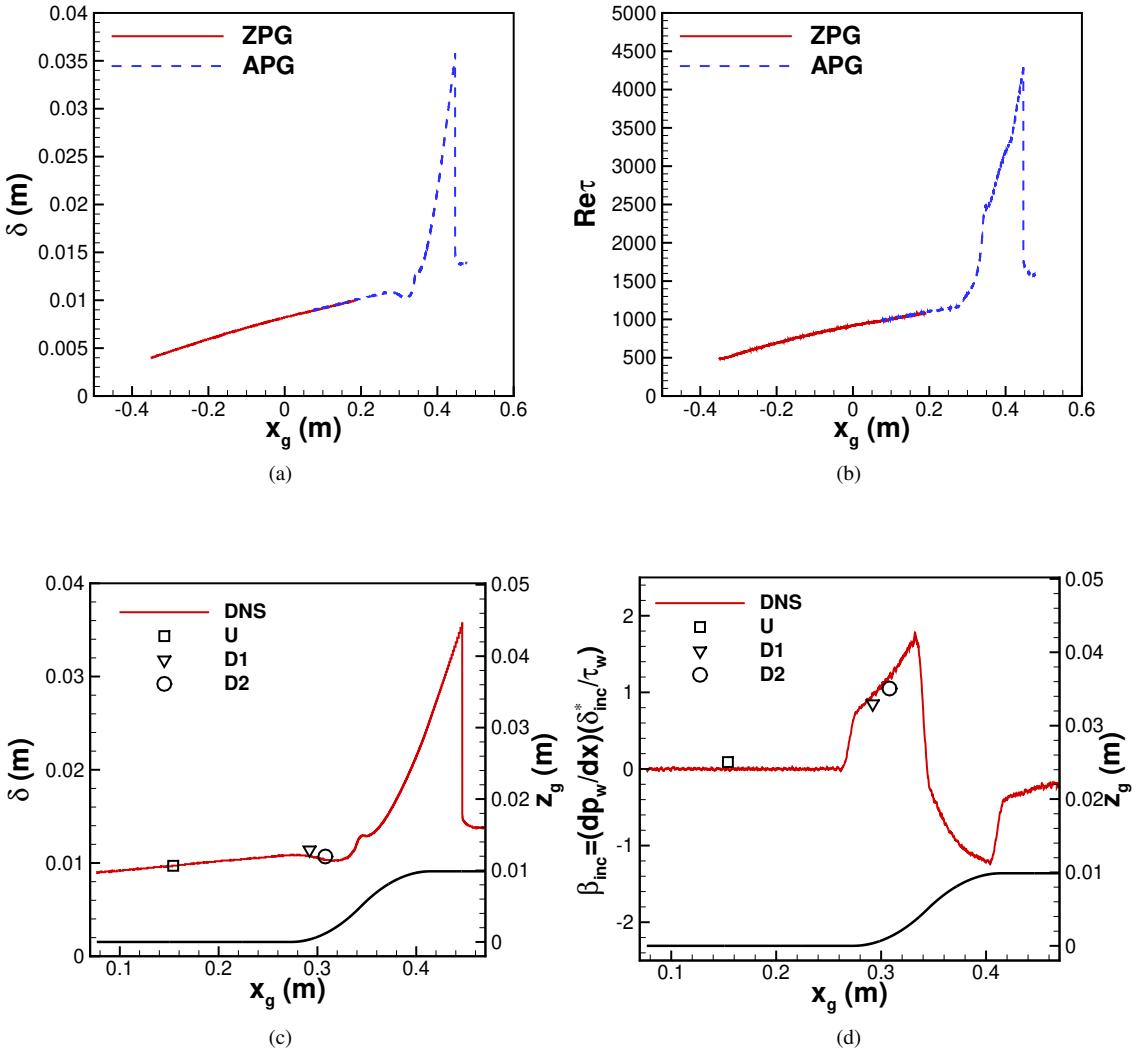

Fig. 3 Evolution of boundary-layer parameters with the axial coordinate x_g, (a) boundary-layer thickness δ; (b) friction Reynolds number Re_τ; (c) boundary-layer thickness δ; (d) Clauser equilibrium pressure gradient parameter β_{inc}.

IV. DNS Results for Mach 4.9 APG TBLs

In this section, the DNS data is used to evaluate the statistics of the Mach 4.9 APG TBLs, which are compared with TAMU's experiments as well as with other experimental and simulation results to help establish the physical realism and the accuracy of the computed results. The DNS statistics at each streamwise location of interest ($x = x_a$) are obtained by first averaging over a streamwise (axial) window ($[x_a - 0.5\delta_i, x_a + 0.5\delta_i]$) and the spanwise direction for each instantaneous flow field; then, an ensemble average over flow-field snapshots spanning a time interval of $T_f u_\tau/\delta$ is calculated. Statistical convergence is verified by calculating averages over varying streamwise window sizes or over a different number of snapshots and by making sure that the differences in flow statistics among the different data-averaging parameters are negligible (< 1%). Throughout the paper, statistics are reported based on fluctuations around either the standard (Reynolds) averages or the density-weighted (Favre) averages. The standard Reynolds averages are denoted by an overbar, $\overline{f}$, whereas the Favre averages are denoted by a tilde, $\tilde{f} = \overline{\rho f}/\overline{\rho}$; fluctuations around standard and Favre averages are denoted by single and double primes, as with $f' = f - \overline{f}$ and $f'' = f - \tilde{f}$, respectively. For the statistics reported in this article, only small differences (< 3%) have been found between the standard and the density-weighted (Favre) averages. Table 3 lists the values of the mean boundary-layer parameters at the selected locations (U, D1, D2) for statistical analysis.

The Van Driest transformed mean-velocity profile based on the DNS at Location U ($x_g = 0.154$ m) is shown in Figure 4. Here, u^+_{VD} is defined as

$$u^+_{\mathrm{VD}} = \int_0^{\overline{u}^+} (\overline{\rho}/\overline{\rho}_w)^{1/2} d\overline{u}^+. \tag{1}$$

The Van Driest transformed velocity at the ZPG location (U) conforms well with the incompressible law of the wall and has a logarithmic region that is comparable in extent to the simulations of ZPG TBLs by Duan et al. [32] at Mach 5.86, and Schlatter and Örlü [34] at a nearly zero Mach number. The transformed velocity in the outer region of the boundary layer conforms particularly well with the transformed velocity of the TAMU experiment of Tichenor et al. [18]. Additionally, an excellent comparison is seen for the van Driest transformed deficit velocity in Figure 4(b). Here, we compared the DNS profiles at the ZPG location against those from Tichenor et al. [18] whose conditions better match the DNS conditions than those of Tichenor et al. [20]. We found that the measured profiles by Tichenor et al. [18] at the ZPG location have some differences from the measurements from Tichenor et al. [20]. Such differences between the two measured profiles are not likely to be caused by the small difference in the freestream conditions alone. We are conducting further investigation to identify the cause behind the discrepancy between the two experimental profiles, so that the impact of those differences on the comparison at the downstream locations can be assessed.

Figure 5 plots the wall-normal profiles of the turbulence intensities and the Reynolds shear stress for Case M5ZPG at Location U ($x_g = 0.154$ m). In general, Morkovin's scaling [44] leads to a good collapse among the data across a wide range of Mach numbers, consistent with the previous experimental and computational observations of ZPG TBLs [18, 45–47]. The streamwise Reynolds-stress based on the current DNS compares very well with the PIV measurements of Tichenor et al. [18] and Williams et al. [47]. However, the wall-normal component of turbulence intensity and the Reynolds shear stress based on the PIV measurements [47] are significantly smaller than those predicted by the various DNS at high Mach numbers. Such reductions in magnitude are typical of particle-based velocimetry studies of supersonic flows [47]. As noted by Williams et al. [47], this loss in the accuracy of the PIV-derived statistics is largely due to particle response limitations that result in significantly reduced levels of wall-normal velocity fluctuations.

Figure 6 shows the mean-velocity profiles from the DNS at the ZPG location and also at the two APG locations

Table 3 Boundary-layer properties at the sample stations, Location U ($x_g = 0.154$ m), D1 ($x_g = 0.292$ m) and D1 ($x_g = 0.308$ m), selected for the analysis for various DNS cases.

Dataset	x_a, m	Re_θ	Re_τ	$Re_{\delta 2}$	Re^*_τ	H_{12}	δ, mm	z_τ, μm	u_τ, m/s	β	β_{inc}	I_p	I_ϕ
DNS, U	0.154	21674	1060	5008	10046	10.4	9.7	9.2	37	0.03	0.01	0	0
Exp, U	0.154	-	-	-	-	-	7.8	-	-	-	0.09	-	-
DNS, D1	0.292	26411	1280	6100	11317	9.2	10.7	8.4	35.2	3.48	0.96	0.1	0.04
Exp,D1	0.292	-	-	-	-	-	11.4	-	-	-	0.85	-	-
DNS, D2	0.308	30966	1384	7152	11357	6.8	10.3	7.5	34.1	3.69	1.22	0.2	0.07
Exp,D2	0.308	-	-	-	-	-	10.7	-	-	-	1.05	-	-

and compares them with the corresponding measurements from the TAMU experiment. Additionally, results from the simulations of Nicholson et al. [31] for both weak and strong FPG flows are included to allow a comparison between the effects of adverse and favorable pressure gradients. Figure 6(a) indicates that, similar to the experiment, the streamwise velocity profile becomes less full in moving from the ZPG location U to the APG locations D1 and D2. The Van Driest transformed velocity profiles at these locations (Fig. 6(b)) collapse well in the viscous sublayer as well as within the buffer-layer and the log-law regions and compare fairly well with the measured data in this region. However, the DNS profiles within the wake region are somewhat higher in comparison with the experimental results. A partial contributor to this discrepancy may be the small changes in the corresponding freestream conditions. Conversely to the effects of an adverse pressure gradient, the favorable pressure gradient tends to make the velocity profile fuller (Fig. 6(c)), while increasing the log-law intercept and reducing the wake function (Fig. 6(d)).

Figure 7 plots the axial, wall-normal, and shear components of the Reynolds-stress at each sampling location with the corresponding data from the TAMU experiments. Consistent with the findings of the experiment [20], the DNS shows a progressive increase in all components of the Reynolds-stress within the inner part of the boundary layer ($z/\delta < 0.6$) as the flow moves downstream into the APG region. The computed profiles of the axial component of the Reynolds-stress are close to the experimental results at all three locations, with the exception of the near-wall portion of experimental profile at Location U. The latter discrepancy is believed to be due to inaccuracies in the PIV measurement. The DNS predictions for the wall-normal component of the Reynolds stress are consistently higher than the measured values, and the same is true for the shear stress component at Location U. On the other hand, the DNS-based shear stress agrees quite well with the measurement at Location D1 and is lower than the measured values at location D2. The above differences in the wall-normal and shear components of the Reynolds stress may be related to the previously discussed issues with the PIV measurements.

Figure 8 examines Morkovin's scaling for the turbulence intensities and the Reynolds shear stress. Unlike the good collapse of the ZPG profiles at different Mach numbers and wall temperature ratios in Figure 5, the Reynolds stress profiles at different pressure gradients at the same Mach number do not collapse as well under Morkovin's scaling. The differences across the three sampling locations are particularly striking in the case of the Reynolds shear stress profiles in Fig. 8(d).

Having examined the effects of APG on the velocity fluctuations, we next scrutinize the DNS results for the wall-normal profiles of the streamwise and wall-normal components of the turbulent heat flux. Similar to the Reynolds stress results discussed earlier, the profiles of the wall-normal turbulent heat flux in figure 9(b) indicate an increase in peak values from the upstream profile U to the downstream profiles D1 and D2.

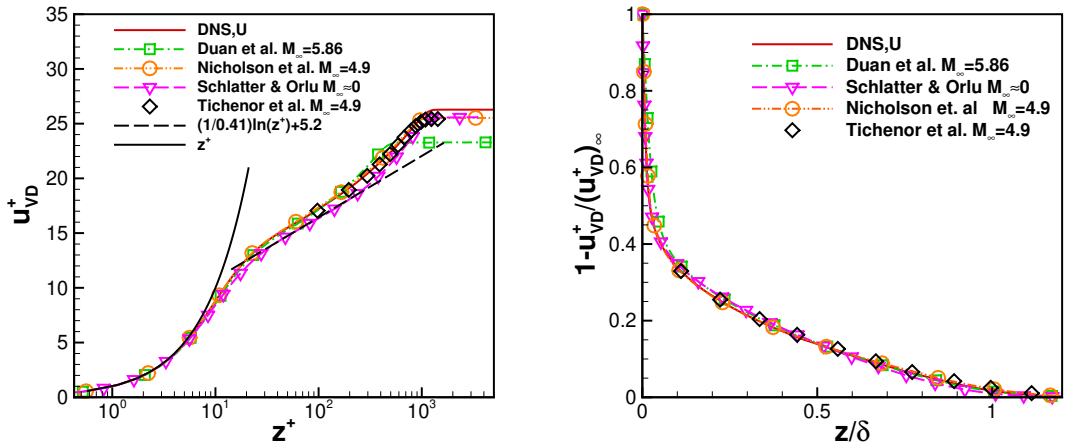

(a) (b)

Fig. 4 (a) Van Driest transformed mean velocity profile and (b) Van Driest transformed mean deficit velocity for the ZPG TBL at Location U ($x_g = 0.154$ m). For comparison, experimental data at the ZPG location for experiments of Tichenor et al. [18] ($M_\infty = 4.9$, $Re_{\delta 2,inc} = 9000$) along with DNS data by Duan et al. [32] ($M_\infty = 5.86$, $Re_\tau = 453$), and Schlatter and Örlü [34] ($M_\infty \approx 0$, $Re_\tau = 1145$) are also plotted in this figure.

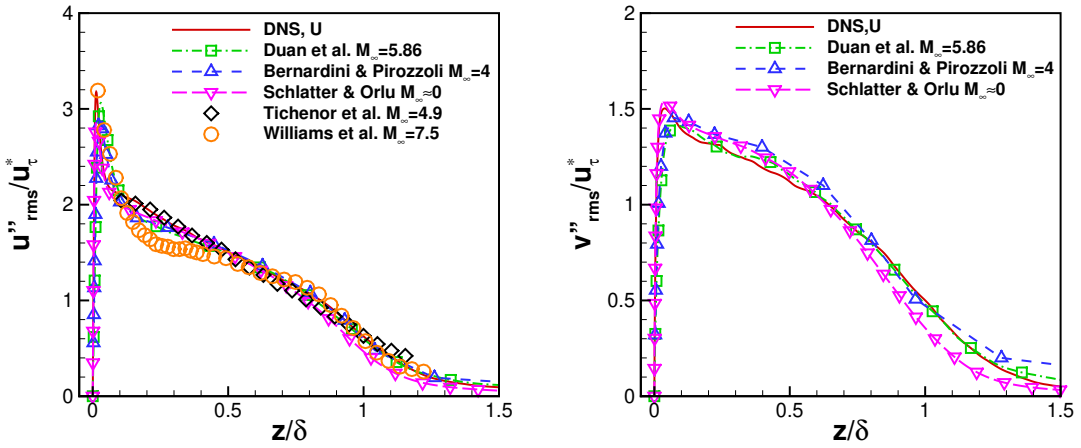

(a) Streamwise turbulence intensity

(b) Spanwise turbulence intensity

(c) Wall-normal turbulence intensity

(d) Reynolds shear stress

Fig. 5 Turbulence intensities and Reynolds shear stress transformed according to Morkovin as a function of wall-normal distance z/δ for the ZPG TBL at Location U ($x_g = 0.154$ m), where $u^* = u_\tau\sqrt{\overline{\rho}_w/\overline{\rho}}$ is the Morkovin transformed velocity scale. For comparison, PIV data by Tichenor [48] ($M_\infty = 4.9$, $Re_{\delta 2,inc} = 9000$) and Williams et al. [47] ($M_\infty = 7.5$, $Re_\tau = 279$) along with DNS data by Duan et al. [32] ($M_\infty = 5.86$, $Re_\tau = 453$), Bernardini and Pirozzoli [33] ($M_\infty = 4.0$, $Re_\tau = 506$), and Schlatter and Örlü [34] ($M_\infty \approx 0$, $Re_\tau = 1145$) are also plotted in this figure.

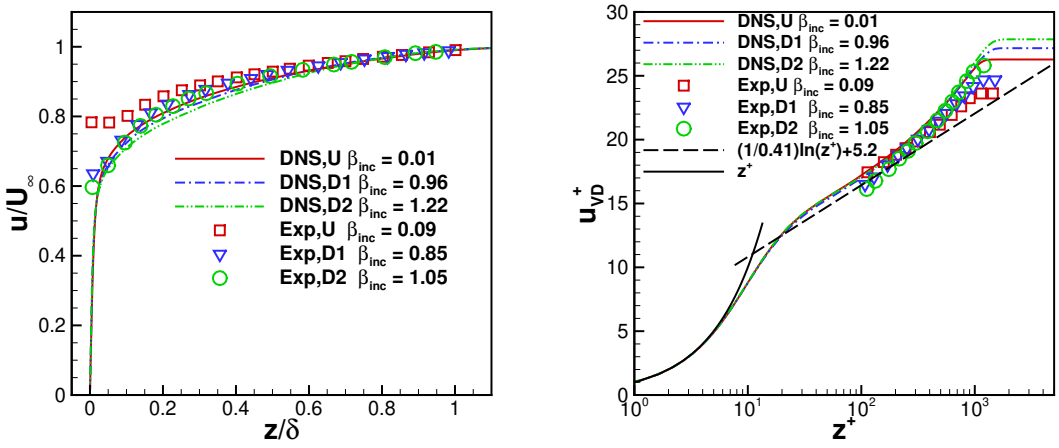

(a) Axial velocity

(b) Van Driest transformed velocity

(c) Axial velocity

(d) Van Driest transformed velocity

Fig. 6 (a/b) Mean velocity distribution at locations U, D1, D2 in comparison with experiments. Symbols represent experimental data of Tichenor et al. [20]. (c/d) Mean velocity distributions compared with weak (WFPG) and strong (SFPG) experiments of Nicholson et al. [31]

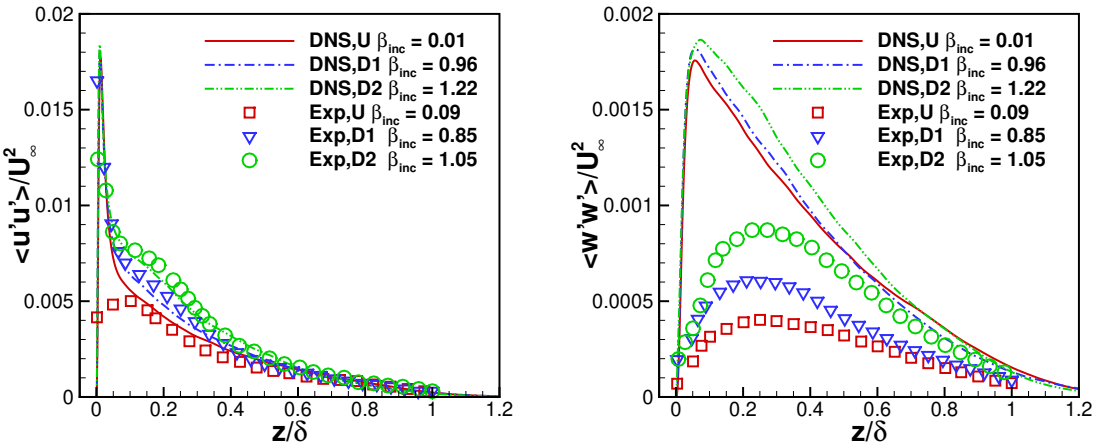

(a) Axial component

(b) Wall-normal component

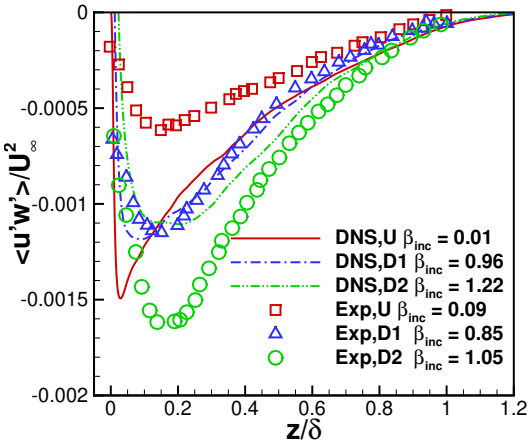

(c) Shear component

Fig. 7 Reynolds-stress profiles at U, D1, D2 locations in comparison with experiments. Symbols represent experiment data of Tichenor et al. [20].

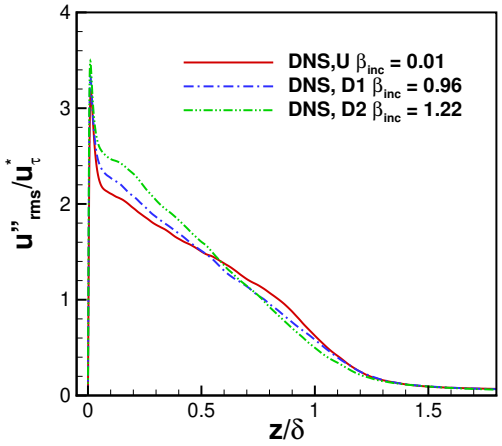

(a) Axial turbulence intensity

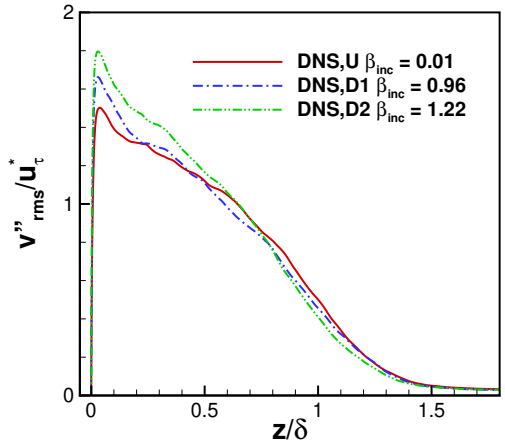

(b) Spanwise turbulence intensity

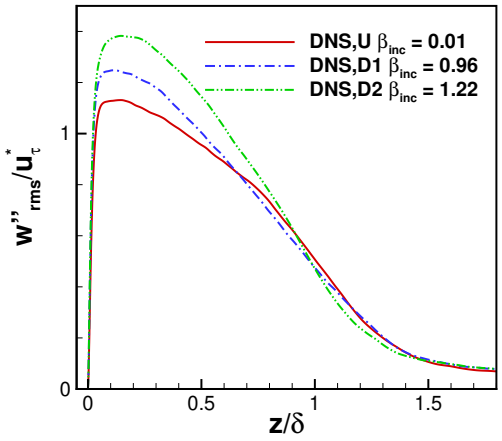

(c) Wall-normal turbulence intensity

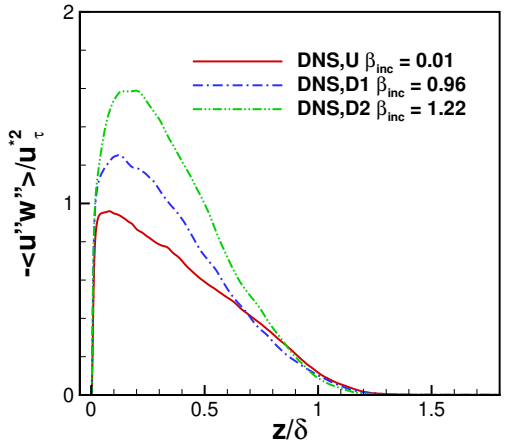

(d) Reynolds shear stress

Fig. 8 Turbulence intensities and Reynolds shear stress transformed according to Morkovin as a function of wall-normal distance z/δ for locations U, D1, D2.

One of the important modeling parameters is the turbulent Prandtl number, which is defined as

$$Pr_t \equiv \frac{\overline{\rho u'' w''}(\partial \tilde{T}/\partial z)}{\overline{\rho w'' T''}(\partial \tilde{u}/\partial z)}. \tag{2}$$

The modified strong Reynolds analogy (SRA) by Huang [49] is given as

$$\frac{T''_{rms}/\tilde{T}}{(\gamma-1)M_\infty^2(u''_{rms}/\tilde{u})} \approx \frac{1}{Pr_t(1-\partial\tilde{T}_o/\partial T)}. \tag{3}$$

Figure 10 displays the wall-normal profiles of the turbulent Prandtl number and the ratio of the left-hand side of Eq. 3 to its right-hand side. Consistent with the previous studies of ZPG TBLs [43, 45, 46, 50], Pr_t is close to unity across most of the boundary layer at the ZPG location. Figure 10(a) shows that the same observation also holds for the two APG locations D1 and D2, which also show minimal difference with respect to the ZPG values for the SRA (Fig. 10(b)). These results indicate that the pressure gradient has little effect on either Pr_t or the SRA ratio from Eq. 3.

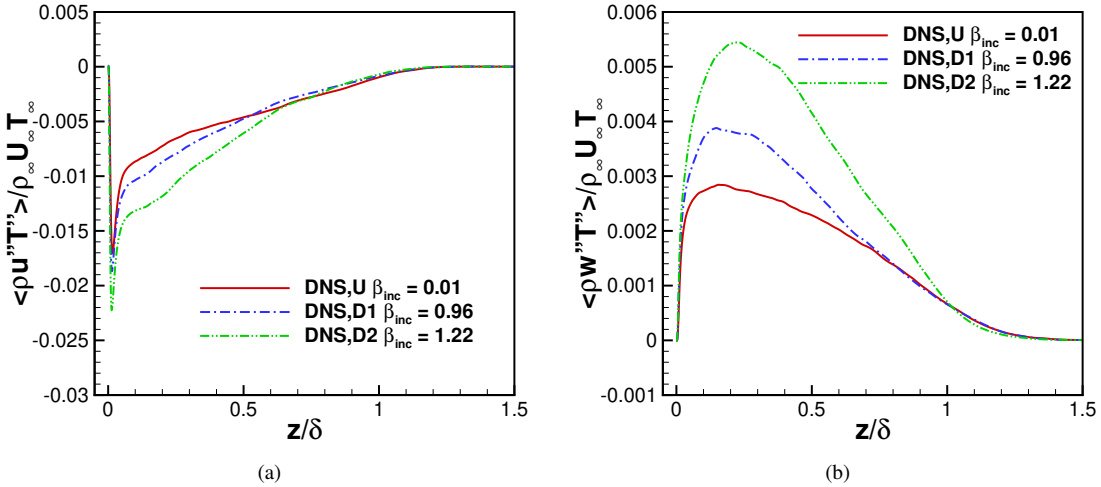

Fig. 9 Turbulent heat-flux distribution of the three locations (U, D1, and D2), (a) the streamwise turbulent heat-flux; (b) the wall-normal turbulent heat-flux.

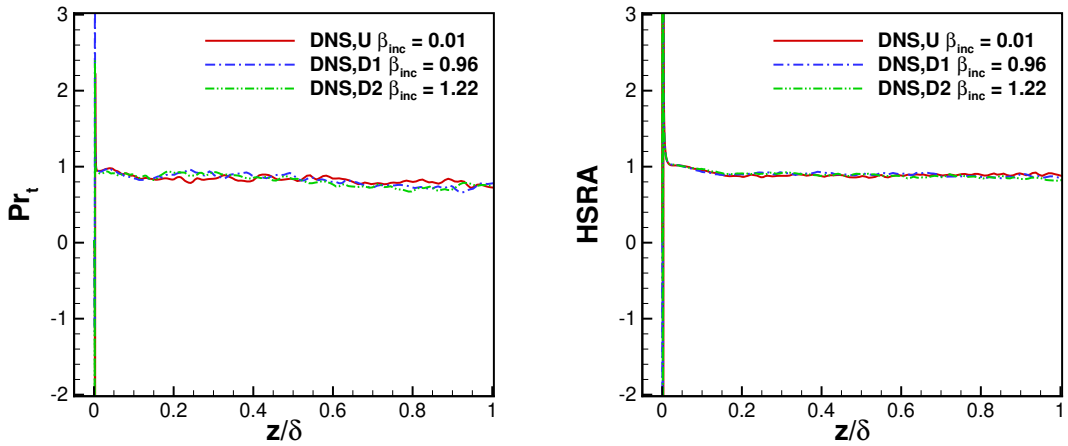

(a) (b)

Fig. 10 Evaluation of strong Reynolds analogy of the three locations (U, D1, and D2), (a) the turbulent Prandtl number Pr_t and (b) the modified SRA of Huang et al. [49].

V. RANS Simulation of Hypersonic Turbulent Boundary Layers

RANS computations were conducted for the ZPG and the APG TBLs with the same flow conditions and thermodynamic equation of state as the DNS cases listed in Table 1. In RANS, NASA's CFL3D code [51] is used to solve the compressible Favre-averaged Navier-Stokes equations [52]. The Favre-averaged RANS equations can be written as:

$$\frac{\partial \overline{\rho}}{\partial t} + \frac{\partial \overline{\rho}\widetilde{u_j}}{\partial x_j} = 0 \tag{4}$$

$$\frac{\partial \overline{\rho}\widetilde{u_i}}{\partial t} + \frac{\partial \overline{\rho}\widetilde{u_i}\widetilde{u_j}}{\partial x_j} = -\frac{\partial \overline{p}}{\partial x_i} + \frac{\partial \overline{\sigma_{ij}}}{\partial x_j} + \frac{\partial \tau_{ij}^T}{\partial x_j} \tag{5}$$

$$\frac{\partial \overline{\rho}\widetilde{E}}{\partial t} + \frac{\partial \overline{\rho}\widetilde{u_i}(\widetilde{E} + \overline{p}/\overline{\rho})}{\partial x_j} = \frac{\partial}{\partial x_j}\left(\overline{\sigma_{ij}}\widetilde{u_i} + \overline{\sigma_{ij}u_i''}\right) - \frac{\partial}{\partial x_j}\left(\overline{q_j} + q_j^T - \widetilde{u_i}\tau_{ij}^T + \frac{1}{2}\overline{\rho u_i'' u_i'' u_j''}\right) \tag{6}$$

where $\widetilde{E} = \widetilde{e} + \frac{1}{2}\widetilde{u_i}\widetilde{u_i} + k^T$, $\overline{q_j} \approx \frac{C_p\widetilde{\mu}}{Pr}\frac{\partial \widetilde{T}}{\partial x_j}$, and $\overline{\sigma_{ij}} \approx 2\widetilde{\mu}\left(\widetilde{S_{ij}} - \frac{1}{3}\frac{\partial \widetilde{u_k}}{\partial x_k}\delta_{ij}\right)$.

In the one- and two-equation turbulence models used herein, the Reynolds stress term $\tau_{ij}^T = -\overline{\rho u_i'' u_j''}$ is modeled by the Boussinesq approximation:

$$\tau_{ij}^T = -\overline{\rho u_i'' u_j''} = 2\mu_t\left(\widetilde{S_{ij}} - \frac{1}{3}\frac{\partial \widetilde{u_k}}{\partial x_k}\delta_{ij}\right) - \frac{2}{3}\rho k^T \delta_{ij} \tag{7}$$

where $\widetilde{S_{ij}}$ is the mean strain, and μ_t is the eddy viscosity obtained via either of the turbulence models, and k^T denotes the turbulent kinetic energy. In the current study, we consider two representative turbulence models that are in widespread use within the aerospace community, namely, the one-equation model of Spalart–Allmaras [53] and the shear-stress transport k-ω model by Menter [54]. Unless otherwise mentioned, the "standard" form" (i.e., the original published form) of the model equations was used, and the details of the model formula and the various coefficients may be found in Refs. [55–57].

The turbulent heat flux term $q_i^T = \overline{\rho h'' u_i''}$ was modeled either by assuming a constant turbulent Prandtl number or via an algebraic model for the turbulent energy flux that was developed by Bowersox [35]. In the constant Prandtl number model, the turbulent heat flux term is modeled as:

$$q_i^T = \overline{\rho h'' u_i''} \approx -\frac{C_p\widetilde{\mu_t}}{Pr_t}\frac{\partial \widetilde{T}}{\partial x_i} \tag{8}$$

where the turbulent Prandtl number Pr_t is assumed to be a constant, and is set equal to 0.9. The algebraic model of Bowersox [35, 58] is based on a simplified form of the transport equation for the energy flux $\theta_i^T = \overline{\rho e'' u_i''}$:

$$\begin{aligned} a_{ik}\theta_k^T &= b_i \\ a_{ik} &= \left[\frac{1}{\tau_\theta} + \frac{R}{C_v}\frac{\partial \widetilde{u_m}}{\partial x_m}\right]\delta_{ik} + \frac{\partial \widetilde{u_i}}{\partial x_k} \\ b_i &= \tau_{ik}^T\left(\frac{\partial \widetilde{h}}{\partial x_k} - \frac{1}{\overline{\rho}}\frac{\partial \overline{p}}{\partial x_k}\right) + \frac{1}{\overline{\rho}}\left(\tau_{kl}^T\frac{\partial \widetilde{u_l}}{\partial x_k}\right)\frac{\partial \overline{p}}{\partial x_i}\tau_e. \end{aligned} \tag{9}$$

Here, $\tau_\theta = \sigma_\theta\tau_u$ and $\tau_e = \sigma_e\tau_u$ are time scales that are proportional to the turbulence time scale $\tau_u = k^T/\epsilon$ as in the $k-\epsilon$ model, and the Reynolds stress term τ_{ik}^T can be modeled by the selected turbulence model. Once θ_i^T is calculated using Eq. 9, the turbulent energy flux $q_i^T = \overline{\rho h'' u_i''}$ can be found as $q_i^T = \gamma\theta_i^T$. Additionally, the streamwise turbulent heat flux q_1^T is modified by a damping function, $d_1 = 1 - exp(-z^*/C_1^+)$, such that $q_1^T = \gamma\theta_1^T/d_1$ to help with its near-wall behavior. Table 4 summarizes the model constants used in the evaluation of Bowersox's algebraic energy flux model.

The terms associated with molecular diffusion $\overline{\sigma_{ij}u_i''}$ and turbulent transport $-\frac{1}{2}\overline{\rho u_i'' u_i'' u_j''}$ within the Favre-averaged energy equation are neglected in the current study [59]. Similar to the DNS, ideal gas relations were used in the RANS computations with air as the working fluid, and Sutherland's law was used for molecular viscosity. A constant molecular Prandtl number of 0.71 is used for calculating the molecular thermal conductivity.

Table 4 Model Constants used for the Bowersox Model.

σ_θ	σ_e	C_1^+	a_1	c_μ
$0.28/\gamma$	$0.4/\gamma$	90	0.28	0.09

Figure 11 shows the schematics of the computational domains for the ZPG and the APG geometries, respectively, along with the boundary conditions used in each case. Informatation on the grid resolution and domain size can be found in table 5. The RANS mesh employs a hyperbolic tangent distribution in the wall normal direction to cluster the grid near the wall, while a uniform grid distribution is used in the streamwise direction.

To monitor potential sensitivity to grid resolution, a grid study was conducted for the $k-\omega$ SST model by comparing the results obtained with the baseline grid and those based on a refined grid with twice the baseline grid resolution in each direction. The two grids yielded very close results as shown in Figure 12. The difference in C_f between the baseline grid and the refined grid is less than 4.0 percent over the entire domain. Because the same inflow was used for the two cases with and without wall curvature, respectively, the C_f values for the ZPG and APG cases match within the upstream part of the computational domain, until the start of the curved wall region at $x = 0.2731$ m.

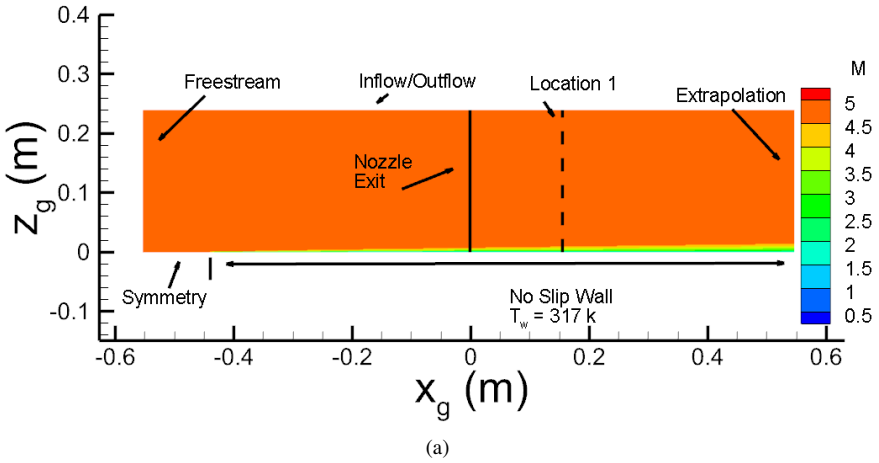

(a)

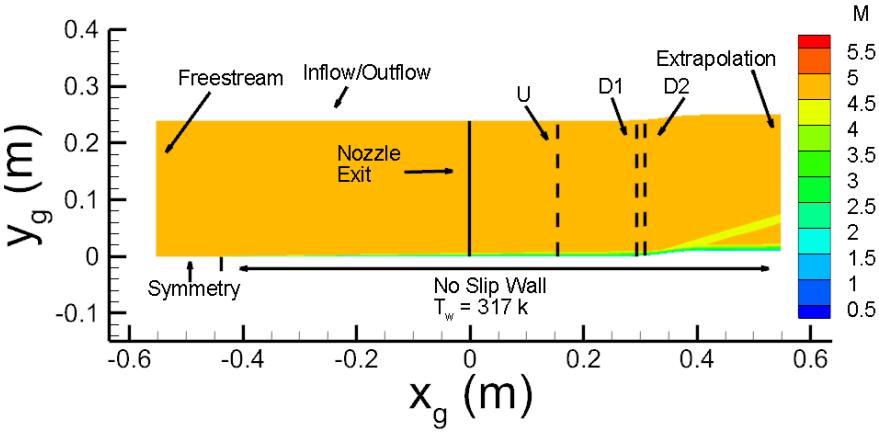

(b)

Fig. 11 Schematics of RANS domains for Cases M5ZPG and M5APG, respectively, along with the boundary conditions.

Table 5 Grid resolution and domain sizes for RANS cases. Here, grid spacing quantities are nondimensionalized by the z_τ evaluated at Location U. z_{min} refers to the first grid spacing, while z_{max} refers to the grid spacing at the boundary-layer edge.

Case	$L_x \times L_y \times L_z$ (m)	x range (m)	$N_x \times N_y \times N_z$	Δx^+	Δz^+_{min}	Δz^+_{max}
RANS-ZPG	$1.1 \times 1 \times 0.24$	-0.553 - 0.547	$857 \times 2 \times 385$	146.5	0.186	22.3
RANS-APG	$1.1 \times 1 \times 0.24$	-0.553 - 0.547	$857 \times 2 \times 385$	146.5	0.186	22.3

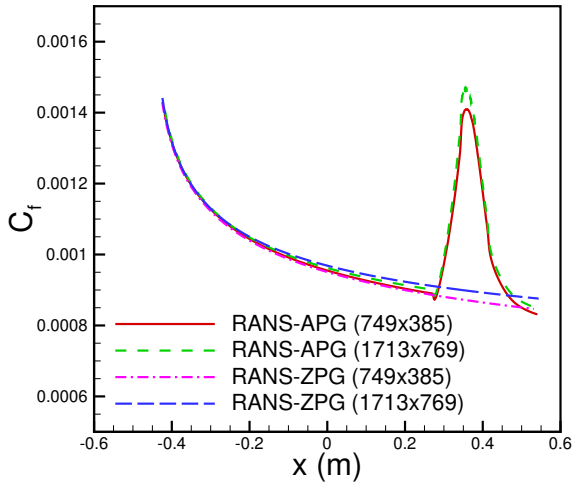

Fig. 12 Grid sensitivity study for the skin-friction coefficients for the ZPG and APG cases, respectively, as obtained with with the $k-\omega$ SST model .

A. A Priori Study of Turbulent Heat Flux Models

In this section, we present the results of an a priori study to assess the turbulent heat-flux predictions based on both the commonly used assumption of a constant turbulent Prandtl number and the AEF model of Bowersox [35, 58]. The results of this study are summarized in figure 13. While the constant Pr_t assumption provides a good comparison with DNS for the wall normal turbulent heat-flux regardless of the local pressure gradient, it fails to capture the streamwise turbulent heat-flux. Regardless of pressure gradient, the constant Prandtl number assumption predicts essentially zero streamwise turbulent heat-flux despite the fact that it is nearly an order of magnitude greater than the wall-normal component. On the other hand, the advanced algebraic energy flux (AEF) model is able to capture the streamwise component reasonably well, while maintaining a satisfactory accuracy of the wall-normal component. This particular finding highlights the potential benefit of the AEF model.

B. A Posteriori Study of RANS Modeling for Hypersonic APG TBLs

This section presents comparisons involving RANS computations of hypersonic boundary layers under an adverse pressure gradient. Specifically, common eddy viscosity models based on a constant turbulent Prandtl number of 0.9 are assessed by comparing the RANS predictions against the DNS data set.

Figure 14 shows a comparison of the predicted skin friction evolution of each model against the results from the DNS. Within the zero pressure gradient, all models give reasonable predictions with the $k-\omega$ SST model providing the best comparison with the DNS data. Moving into the APG region, both the SA and $k-\omega$ SST models continue to give DNS-like predictions while the Baldwin Lomax model shows a delayed increase in predicted skin friction. As flow moves into the favorable pressure gradient region, the $k-\omega$ SST continues to provide excellent comparison with DNS. Additionally, the skin friction predicted by the method of Van Driest II [60] compares excellently within the ZPG region, but fails to capture the increase in skin friction due to the pressure gradient.

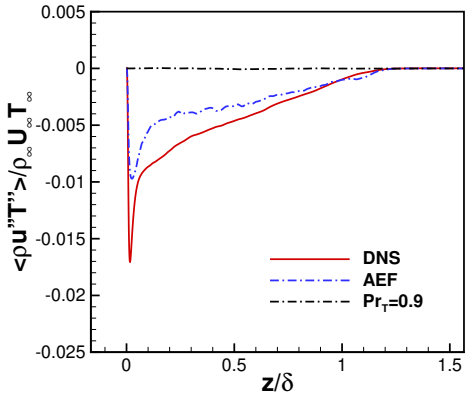

(a) Location U ($x_g = 0.154m$)

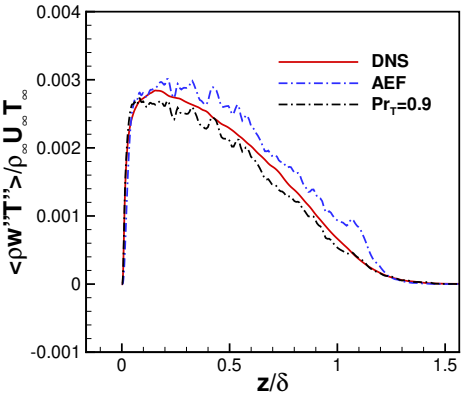

(b) Location U ($x_g = 0.154m$)

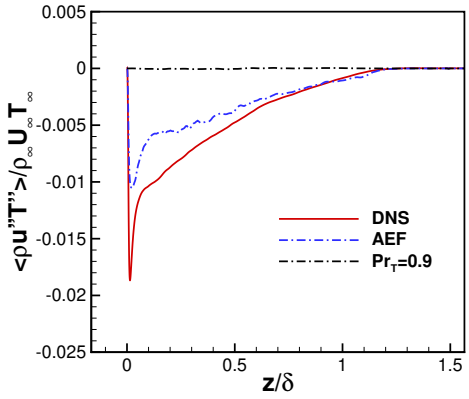

(c) Location D1 ($x_g = 0.292m$)

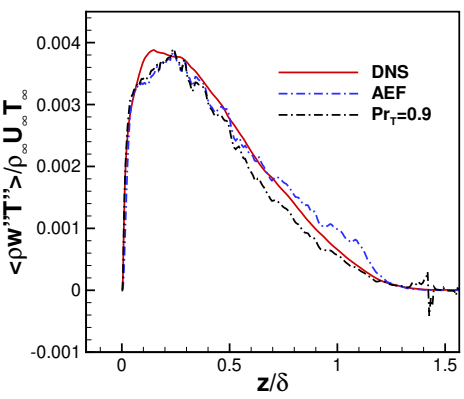

(d) Location D1 ($x_g = 0.292m$)

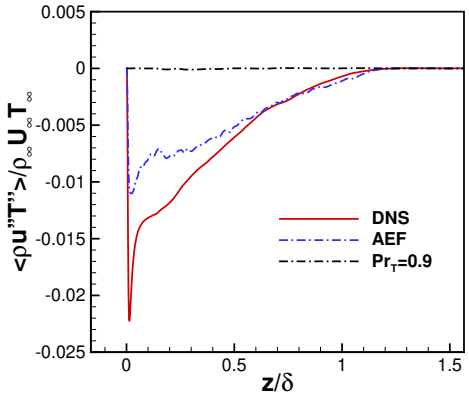

(e) Location D2 ($x_g = 0.308m$)

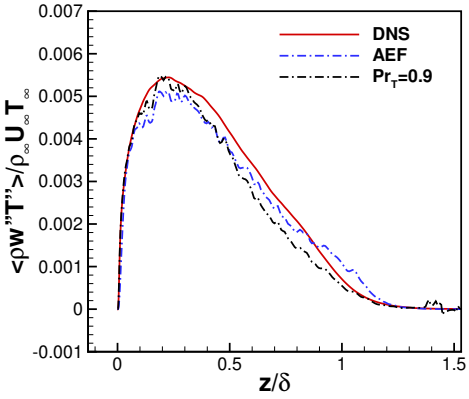

(f) Location D2 ($x_g = 0.308m$)

Fig. 13 A priori comparison of the turbulent heat-flux calculated using an assumption of constant turbulent Prandtl number of 0.9 with the DNS results, for (a/c/e) Streamwise turbulent heat-flux; (b/d/f) Wall-normal turbulent heat-flux.

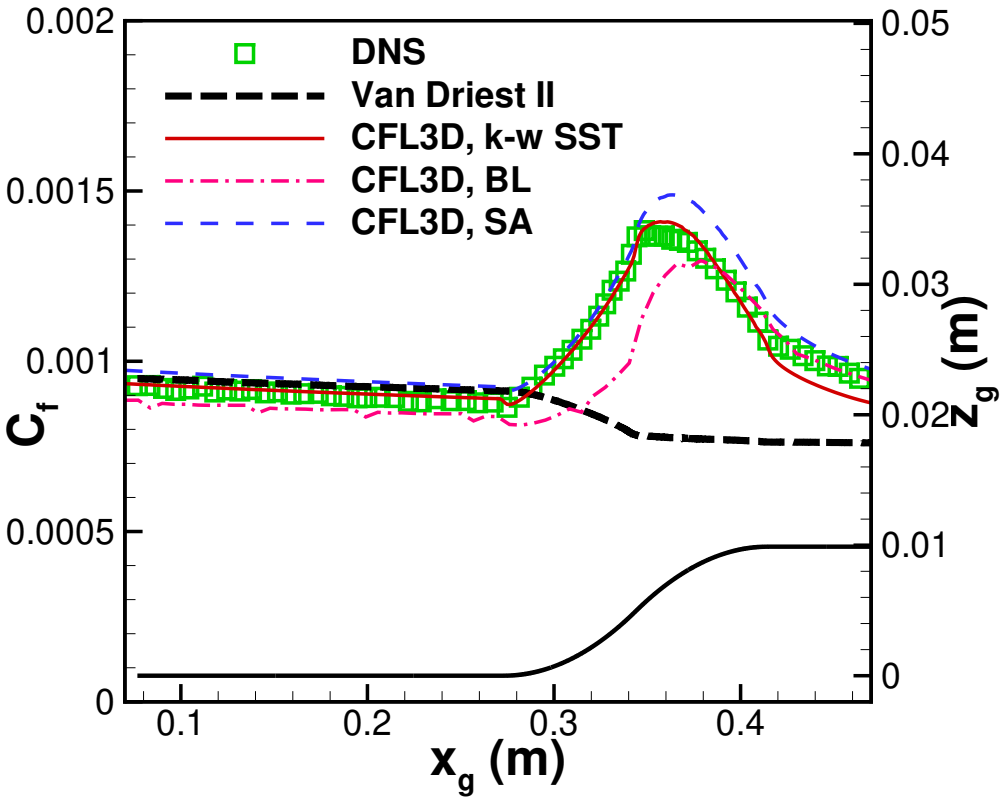

Fig. 14 Streamwise development of C_f predicted by DNS and RANS. The right vertical axis plots the z to visualize the shape of the wall.

The predicted velocity profiles at locations D1 and D2 are compared with DNS results in FIG. 15. Here both the SA and $k-\omega$ SST models compare well with DNS results, while the Baldwin Lomax model predicts an increased wake function and larger defect throughout the boundary layer.

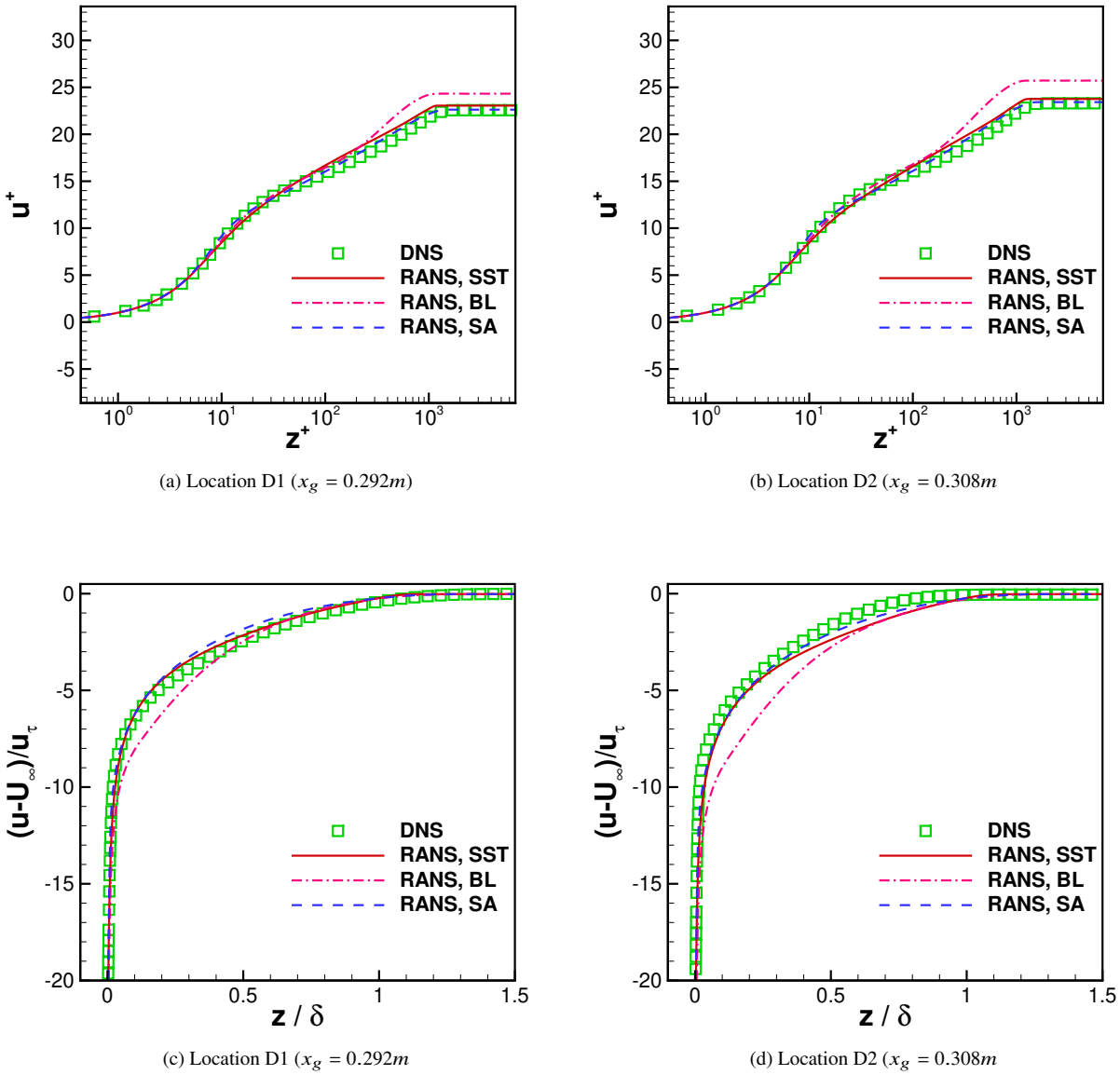

(a) Location D1 ($x_g = 0.292m$)

(b) Location D2 ($x_g = 0.308m$

(c) Location D1 ($x_g = 0.292m$

(d) Location D2 ($x_g = 0.308m$

Fig. 15 Comparison of mean velocity profiles obtained from DNS and at Locations D1 and D2. The profiles are normalized using (a/b) inner scaling and (c/d) defect-law scaling.

Figure 16 shows a comparison of the Reynolds stress profiles based on the RANS models mentioned earlier. The Reynolds stresses were calculated using the Boussinesq assumption (Eq. 7). Here the streamwise Reynolds stress, $(\widetilde{u''u''})$, is significantly underpredicted in the near wall region by the various RANS models, while the wall-normal Reynolds-stress, $(\widetilde{w''w''})$, is overpredicted by each model. For the Reynolds shear stress, $(\widetilde{u''w''})$, the SA and Baldwin Lomax models give excellent predictions at location D1, while the $k-\omega$ SST model slightly underpredicts the Reynolds shear stress. At location D2, which has a greater pressure gradient, the predictions of all models are found to worsen significantly.

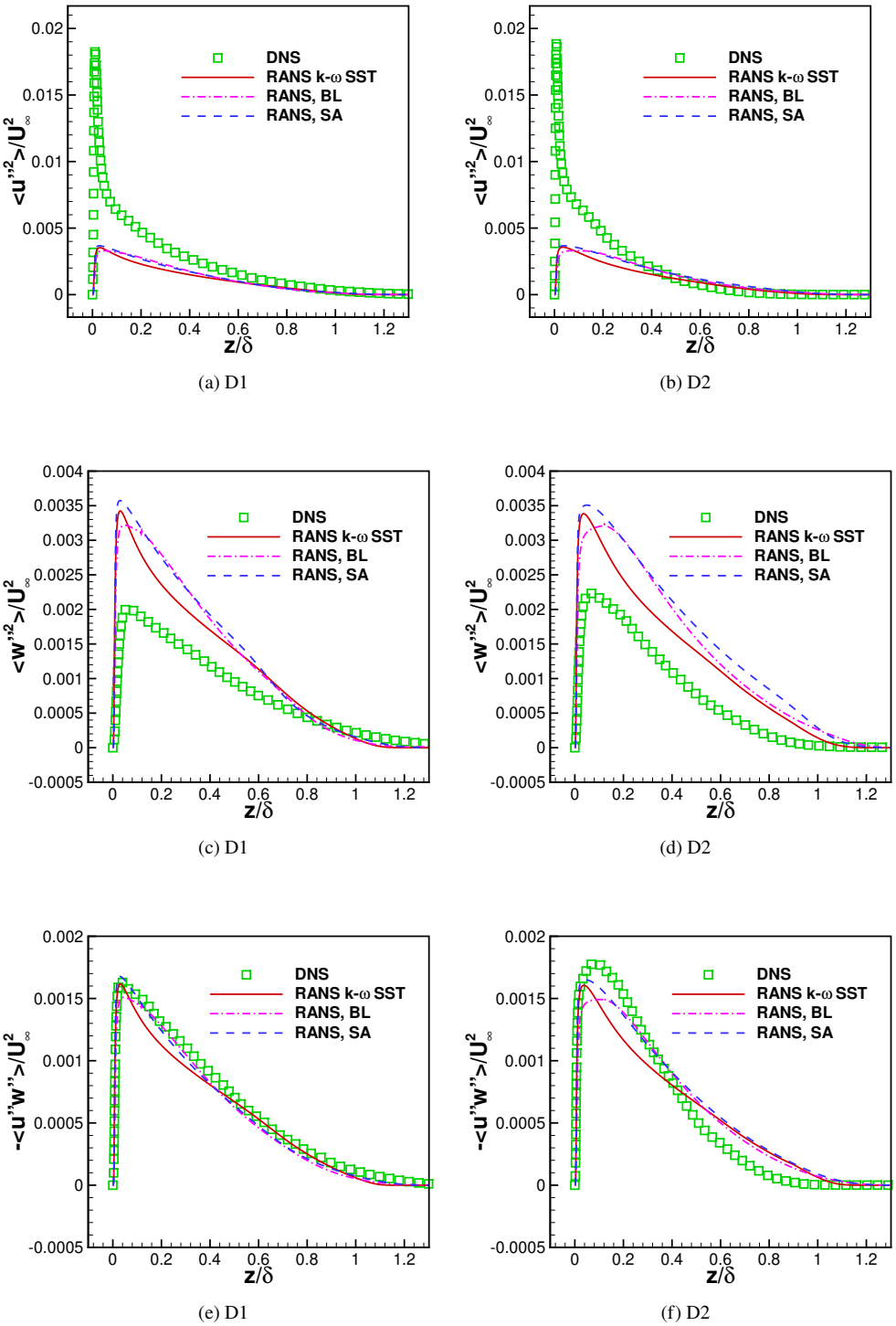

(a) D1 (b) D2

(c) D1 (d) D2

(e) D1 (f) D2

Fig. 16 Comparison of Reynolds-stress profiles from RANS and DNS at locations D1 and D2, (a/b) streamwise component $\overline{u'^2}/U_\infty^2$, (c/d) wall-normal component $\overline{w'^2}/U_\infty^2$, (e/f) shear stress $-\overline{u'w'}/U_\infty^2$ velocity in outer scale, symbols represent experimental data of Tichenor et al. [18].

VI. Summary

This paper has presented the results of an ongoing computational study that is aimed at evaluating the accuracy of commonly utilized Reynolds-averaged Navier-Stokes (RANS) models in predicting high-speed, turbulent boundary-layers developing under nonzero pressure gradients. Specifically, we have extended the findings of the previous studies for a Mach 5 boundary layer encountering favorable pressure gradients [31] to include the effects of an adverse pressure gradient. To help evaluate the RANS models for such flows, the RANS predictions were compared with a new, detailed numerical dataset based on the direct numerical simulation (DNS) of a Mach 5 experimental flow configuration. The experiment had been performed in the National Aerothermochemistry Laboratory (NAL) at the Texas A&M University, and the measurements included data within both a zero pressure gradient region and for adverse pressure gradients due to suitably designed surface curvature.

The DNS has been validated against the experimental results of Tichenor et al. [18, 20], as well as through selective comparisons with several other DNS datasets for a zero pressure gradient boundary layer [32–34]. The DNS results agree well with the velocity profiles measured by Tichenor et al. [18, 20]. Within the zero pressure gradient region, the Van Driest II transformed velocity profiles reveal good collapse with other DNS results across a broad range of Mach numbers. For a boundary layer developing under an adverse pressure gradient, the DNS results show a similarly good collapse; however, the DNS predicts a slightly higher wake function than that inferred from the experimental measurements [20]. DNS results for the zero-pressure-gradient case indicate that Morkovin's scaling [44] leads to a good collapse of the streamwise and spanwise turbulence intensities from the present DNS with the corresponding data from other DNS at different values of the flow Mach number. On the other hand, the PIV data from the experiment show a reduced magnitude of the wall-normal turbulent intensity and the Reynolds stress when compared to the DNS results. This reduction is typical of PIV measurement studies of supersonic flows [47]. For the flow developing under an adverse pressure gradient, we found that Morkovin's scaling does not provide a good collapse for turbulence intensities. In general, the predicted streamwise Reynolds stress compares well with the experimental results of Tichenor et al. [20]. However, experimental results report a generally lower magnitude for the wall-normal and shear Reynolds stresses. The DNS predicts a significant increase in both the Reynolds stresses and the turbulent heat flux values for increasing pressure gradient. Additionally, the constant Prantdl number assumption as well as Huang's [49] version of the strong Reynolds analogy are shown to be adequate for both zero and adverse pressure gradients corresponding to incompressible Clauser pressure gradient parameter β_{inc} of up to at least 1.22.

The predictions of the Baldwin-Lomax (BL), Spalart-Allmaras (SA) and the $k-\omega$ SST turbulence models were evaluated against the DNS data set. The comparisons showed that for β_{inc} values of at least up to 1.22, the BL and SA models were able to provide adequate predictions for skin friction, and the $k-\omega$ SST model was able to yield DNS-like predictions for the bulk of the flow. Overall, within the range of the TAMU experiment, the adverse pressure gradients has little impact on the accuracy of these models, and the Boussinesq assumption provided reasonable predictions for the Reynolds shear stress. However, the Boussinesq assumption failed to adequately predict the streamwise and wall-normal Reynolds stresses.

In addition to the evaluation of the Reynolds stress predictions based on the eddy viscosity models, the predictions of the turbulent heat flux based on the commonly used assumption of a constant turbulent Prandtl number and, also, on the more advanced algebraic energy flux (AEF) model of Bowersox [35, 58] are compared with the DNS results. While both types of models were found to yield good predictions of the wall-normal component of the turbulent heat flux, the assumption of a constant Prandtl number failed to provide adequate predictions of the streamwise turbulent heat flux. On the other hand, the AEF model was able to provide improved predictions of both wall-normal and streamwise components, highlighting the potential of that model for aeroheating predictions for high-speed configurations.

Acknowledgments

The authors would like to thank Dr. Rodney Bowersox and his group for valuable discussions. Additionally, the authors (Gary L. Nicholson, Junji Huang, and Lian Duan) would like to acknowledge financial support by the Office of Naval Research (under grant N00014-20-1-2194, managed by Dr. Eric Marineau) and the National Science Foundation (under grant CBET 2001127, managed by Dr. Ron Joslin). Author M. Choudhari was supported by the NASA Hypersonic Technology Project. Computational resources were provided by the DoD High Performance Computing Modernization Program and the Ohio Supercomputer Center. The views and conclusions contained herein are those of the authors and should not be interpreted as necessarily representing the official policies or endorsements, either expressed or implied, of the funding agencies or the U.S. Government.

References

[1] Bradshaw, P., "The analogy between streamline curvature and buoyancy in turbulent shear flow," *Journal of Fluid Mechanics*, Vol. 36, 1969, pp. 177–191.

[2] Bradshaw, P., "The effect of mean compression or dilatation on the turbulence structure of supersonic boundary layers," *Journal of Fluid Mechanics*, Vol. 63, 1974, pp. 449–464.

[3] Lee, J.-H., and Sung, H. J., "Structures in Turbulent Boundary Layers Subjected to Adverse Pressure Gradients," *Journal of Fluid Mechanics*, Vol. 639, 2009, pp. 101–131.

[4] Schlatter, P., and Örlü, R., "Assessment of Direct Numerical Simulation Data of Turbulent Boundary Layers," *Journal of Fluid Mechanics*, Vol. 659, 2010, pp. 116–126. doi:10.1017/S0022112010003113.

[5] Vila, C. S., Örlü, R., Vinuesa, R., Schlatter, P., Ianiro, A., and Discetti, S., "Adverse-pressure-gradient effects on turbulent boundary layers: statistics and flow-field organization," *Flow, Turbulence and Combustion*, Vol. 99, No. 3-4, 2017, pp. 589–612.

[6] Bobke, A., Vinuesa, R., Örlü, R., and Schlatter, P., "Large-eddy simulations of adverse pressure gradient turbulent boundary layers," *Journal of Physics: Conference Series*, Vol. 708, IOP Publishing, 2016, p. 012012.

[7] Bobke, A., Vinuesa, R., Örlü, R., and Schlatter, P., "History effects and near equilibrium in adverse-pressure-gradient turbulent boundary layers," *Journal of Fluid Mechanics*, Vol. 820, 2017, pp. 667–692.

[8] Jayaram, M., Taylor, M. W., and Smits, A. J., "The response of a compressible turbulent boundary layer to short regions of concave surface curvature," *Journal of Fluid Mechanics*, Vol. 175, 1987, pp. 343–362.

[9] Donovan, J. F., Spina, E. F., and Smits, A. J., "The structure of a supersonic turbulent boundary layer subjected to concave surface curvature," *Journal of Fluid Mechanics*, Vol. 259, 1994, pp. 1–24.

[10] Spina, E. F., Smits, A. J., and Robinson, S. K., "The Physics of Supersonic Turbulent Boundary Layers," *Annual Review of Fluid Mechanics*, Vol. 26, 1994, pp. 287–319.

[11] Smith, D. R., and Smits, A. J., "A Study of the effects of curvature and compression on the behavior of a supersonic turbulent boundary layer," *Experiments in Fluids*, Vol. 18, 1995, pp. 363–369.

[12] Arnette, S., Samimy, M., and Elliott, G., "Structure of supersonic turbulent boundary layer after expansion regions," *AIAA Journal*, Vol. 33, No. 3, 1995, pp. 430–438.

[13] Arnette, S., Samimy, M., and Elliott, G., "The effects of expansion on the turbulence structure of compressible boundary layers," *Journal of Fluid Mechanics*, Vol. 367, 1998, pp. 67–105.

[14] Smits, A. J., and Dussauge, J. P., *Turbulent Shear Layers in Supersonic Flow*, 2nd ed., Springer-Verlag New York, 2006. doi:10.1007/b137383.

[15] Luker, J., Bowersox, R. D. W., and Buter, T., "Influence of curvature-driven favourable pressure gradient on supersonic turbulent boundary layer," *AIAA Journal*, Vol. 38, No. 8, 2010, pp. 1351–1359.

[16] Ekoto, I. W., Bowersox, R. D. W., Beutner, T., and Goss, L., "Response of Supersonic Turbulent Boundary Layers to Local and Global Mechanical Distortions," *Journal of Fluid Mechanics*, Vol. 630, 2009, pp. 225–265.

[17] Humble, R. A., Peltier, S. J., and Bowersox, R. D. W., "Visualization of the structural response of a hypersonic turbulent boundary layer to convex curvature," *Physics of Fluids*, Vol. 24, 2012, p. 106103.

[18] Tichenor, N. R., Humble, R. A., and Bowersox, R. D. W., "Response of a Hypersonic Turbulent Boundary Layer to Favourable Pressure Gradients," *Journal of Fluid Mechanics*, Vol. 722, 2013, pp. 187–213.

[19] Neel, I., Leidy, A. N., Bowersox, R. D. W., and Tichenor, N. R., "Influence of Favorable Pressure Gradients on a Mach 5.0 Turbulent Boundary Layer," *AIAA Paper 2016-4248*, 2016. `https://doi.org/10.2514/6.2016-4248`.

[20] Tichenor, N. R., Neel, I., Leidy, A., and Bowersox, R. D., "Influence of Streamline Adverse Pressure Gradients on the Structure of a Mach 5 Turbulent Boundary Layer," *AIAA Paper 2017-1697*, 2017. `https://doi.org/10.2514/6.2017-1697`.

[21] Carlson, J. D., Bowersox, R. D. W., and Tichenor, N. R., "Proper Orthogonal Decomposition Analysis of Hypersonic Turbulent Boundary Layers Subjected to Streamline Wall Curvature," *AIAA Paper 2020-2060*, 2020.

[22] Wang, Q., Wang, Z., and Zhao, Y., "An experimental investigation of the supersonic turbulent boundary layer subjected to concave curvature," *Phys. Fluids*, Vol. 28, 2016, p. 096104.

[23] Wang, Q., and Wang, Z., "Structural characteristics of the supersonic turbulent boundary layer subjected to concave curvature," *Appl. Phys. Lett.*, Vol. 108, 2016, p. 114102.

[24] Wang, Q.-C., Wang, Z.-G., and Zhao, Y.-X., "On the impact of adverse pressure gradient on the supersonic turbulent boundary layer," *Physics of Fluids*, Vol. 28, No. 11, 2016, p. 116101.

[25] Wang, X., Wang, Z., Sun, M., Wang, Q., and Hu, Z., "Direct numerical simulation of a supersonic turbulent boundary layer subject to adverse pressure gradient induced by external successive compression waves," *AIP Advances*, Vol. 9, No. 8, 2019, p. 085215.

[26] Sun, M., Sandham, N. D., and Hu, Z., "Turbulence structures and statistics of a supersonic turbulent boundary layer subjected to concave surface curvature," *Journal of Fluid Mechanics*, Vol. 865, 2019, pp. 60–99.

[27] Wang, X., Wang, Z., Sun, M., Wang, Q., and Hu, Z., "Effects of favorable pressure gradient on turbulence structures and statistics of a flat-plate supersonic turbulent boundary layer," *Physics of Fluids*, Vol. 32, No. 2, 2020, p. 025107.

[28] Wenzel, C., Peter, J. M., Selent, B., Weinschenk, M. B., Rist, U., and Kloker, M. J., "DNS of compressible turbulent boundary layers with adverse pressure gradients," *High Performance Computing in Science and Engineering'18*, Springer, 2019, pp. 229–242.

[29] Wenzel, C., Gibis, T., Kloker, M., and Rist, U., "Self-similar compressible turbulent boundary layers with pressure gradients. Part 1. Direct numerical simulation and assessment of Morkovin's hypothesis," *Journal of Fluid Mechanics*, Vol. 880, 2019, pp. 239–283.

[30] Gibis, T., Wenzel, C., Kloker, M., and Rist, U., "Self-similar compressible turbulent boundary layers with pressure gradients. Part 2. Self-similarity analysis of the outer layer," *Journal of Fluid Mechanics*, Vol. 880, 2019, pp. 284–325.

[31] Nicholson, G., Huang, J., Duan, L., Choudhari, M. M., and Bowersox, R. D., "Simulation and Modeling of Hypersonic Turbulent Boundary Layers Subject to Favorable Pressure Gradients due to Streamline Curvature," *AIAA Scitech 2021 Forum*, 2021, p. 1672.

[32] Duan, L., Choudhari, M. M., and Zhang, C., "Pressure Fluctuations induced by a Hypersonic Turbulent Boundary Layer," *Journal of Fluid Mechanics*, Vol. 804, 2016, pp. 578–607.

[33] Bernardini, M., and Pirozzoli, S., "Wall Pressure Fluctuations Beneath Supersonic Turbulent Boundary Layers," *Physics of Fluids*, Vol. 23, No. 8, 2011, p. 085102.

[34] Schlatter, P., and Örlü, R., "Assessment of direct numerical simulation data of turbulent boundary layers," *Journal of Fluid Mechanics*, Vol. 659, 2010, pp. 116–126.

[35] Bowersox, R. D. W., "Extension of equilibrium turbulent heat flux models to high-speed shear flows," *Journal of Fluid Mechanics*, Vol. 633, 2009, pp. 61–70.

[36] Neel, I. T., Leidy, A., Bowersox, R. D., and Tichenor, N. R., "Hypersonic boundary layer with streamline curvature-driven adverse pressure gradient," *8th AIAA Flow Control Conference*, 2016, p. 4248.

[37] Williamson, J., "Low-Storage Runge-Kutta Schemes," *Journal of Computational Physics*, Vol. 35, No. 1, 1980, pp. 48–56.

[38] Duan, L., Choudhari, M. M., and Wu, M., "Numerical Study of Acoustic Radiation due to a Supersonic Turbulent Boundary Layer," *Journal of Fluid Mechanics*, Vol. 746, 2014, pp. 165–192.

[39] Simens, M. P., Jimenez, J., Hoyas, S., and Mizuno, Y., "A High-resolution Code for Turbulent Boundary Layers," *Journal of Computational Physics*, Vol. 228, No. 11, 2009, pp. 4218–4231.

[40] Thompson, K. W., "Time Dependent Boundary Conditions for Hyperbolic Systems," *Journal of Computational Physics*, Vol. 68, No. 1, 1987, pp. 1–24.

[41] Zhang, C., Duan, L., and Choudhari, M. M., "Effect of Wall Cooling on Boundary Layer Induced Pressure Fluctuations at Mach 6," *Journal of Fluid Mechanics*, Vol. 822, 2017, pp. 5–30.

[42] Zhang, C., Duan, L., and Choudhari, M. M., "Direct Numerical Simulation Database for Supersonic and Hypersonic Turbulent Boundary Layers," *AIAA Journal*, 2018. https://arc.aiaa.org/doi/pdf/10.2514/1.J057296.

[43] Huang, J., Nicholson, G. L., Duan, L., Choudhari, M. M., and Bowersox, R. D. W., "Simulation and Modeling of Cold-Wall Hypersonic Turbulent Boundary Layers on Flat Plate," *AIAA Paper 2020-0571*, 2020.

[44] Morkovin, M. V., "Effects of Compressibility on Turbulent Flows," *In Mécanique de la Turbulence* (ed. A. J. Favre), CNRS, 1962, pp. 367–380.

[45] Duan, L., Beekman, I., and Martín, M. P., "Direct numerical simulation of hypersonic turbulent boundary layers. Part 2: Effect of wall temperature," *Journal of Fluid Mechanics*, Vol. 655, 2010, pp. 419–445.

[46] Duan, L., Beekman, I., and Martín, M. P., "Direct numerical simulation of hypersonic turbulent boundary layers. Part 3: Effect of Mach number," *Journal of Fluid Mechanics*, Vol. 672, 2011, pp. 245–267.

[47] Williams, O. J. H., Sahoo, D., Baumgartner, M. L., and Smits, A. J., "Experiments on the Structure and Scaling of Hypersonic Turbulent Boundary Layers," *Journal of Fluid Mechanics*, Vol. 834, 2018, pp. 237–270.

[48] Tichenor, N. R., "Characterization of the influence of a favorable pressure gradient on the basic structure of a Mach 5.0 high Reynolds number supersonic turbulent boundary layer," Ph.D. thesis, Texas A&M University, College Station, Texas, 2010.

[49] Huang, P. G., Coleman, G. N., and Bradshaw, P., "Compressible Turbulent Channel Flows: DNS Results and Modelling," *Journal of Fluid Mechanics*, Vol. 305, 1995, pp. 185–218.

[50] Duan, L., and Martín, M. P., "Direct Numerical Simulation of Hypersonic Turbulent Boundary Layers. Part 4: Effect of High Enthalpy," *Journal of Fluid Mechanics*, Vol. 684, 2011, pp. 25–59.

[51] Bartels, R. E., Rumsey, C. L., and Biedron, R. T., "CFL3D Version 6.4 - General Usage and Aeroelastic Analysis," Tech. rep., NASA/TM-2006-214301, 2006.

[52] Rumsey, C. L., "Implementing Turbulence Models into the Compressible RANS Equations," Turbulence Modeling Resource," *https://turbmodels.larc.nasa.gov/implementrans.html*, cited 1 January, 2021.

[53] Spalart, P. R., and Allmaras, S. R., "A One-Equation Turbulence Model for Aerodynamic Flows," *Recherche Aerospatiale*, Vol. 1, No. 5, 1994, pp. 5–21.

[54] Menter, F. R., "Two-equation eddy-viscosity turbulence models for engineering applications," *AIAA Journal*, Vol. 32, No. 8, 1994, pp. 1598–1605.

[55] Rumsey, C. L., "The Spalart-Allmaras Turbulence Model," *https://turbmodels.larc.nasa.gov/spalart.html*, cited 1 January, 2021.

[56] Rumsey, C. L., "The Menter Baseline Turbulence Model," *https://turbmodels.larc.nasa.gov/bsl.html*, cited 1 January, 2021.

[57] Rumsey, C. L., "The Menter Shear Stress Transport Turbulence Model," *https://turbmodels.larc.nasa.gov/sst.html*, cited 1 January, 2021.

[58] Bowersox, R. D. W., and North, S. W., "Algebraic Turbulent Energy Flux Models for Hypersonic Shear Flows," *Progress in Aerospace Sciences*, Vol. 46, 2010, pp. 49–61.

[59] "ANSYS® Fluent, Release 18.0, Help System, Theory Guide," *ANSYS, Inc.*, 2018.

[60] Driest, E. V., "On turbulent flow near a wall," *Journal of the aeronautical sciences*, Vol. 23, No. 11, 1956, pp. 1007–1011.